Geophysical Journal International

Geophys. J. Int. (2016) **206,** 574–589
Advance Access publication 2016 April 28
GJI Marine geosciences and applied geophysics

doi: 10.1093/gji/ggw170

Ocean acoustic remote sensing using ambient noise: results from the Florida Straits

M.G. Brown,[1] O.A. Godin,[2,3] X. Zang,[1] J.S. Ball,[2] N.A. Zabotin,[2] L.Y. Zabotina[2] and N.J. Williams[1]

[1]*Rosenstiel School of Marine and Atmospheric Sciences, University of Miami,* 4600 *Rickenbacker Cswy., Miami, FL* 33149, *USA.*
E-mail: mbrown@rsmas.miami.edu
[2]*Cooperative Institute for Research in Environmental Sciences,* 216 *UCB, University of Colorado campus, Boulder, CO* 80309, *USA*
[3]*NOAA Earth System Research Laboratory, Physical Sciences Division, Mail Code R/PSD,* 325 *Broadway, Boulder, CO* 80305, *USA*

Accepted 2016 April 25. Received 2016 April 8; in original form 2015 December 29

SUMMARY

Noise interferometry is the process by which approximations to acoustic Green's functions, which describe sound propagation between two locations, are estimated by cross-correlating time series of ambient noise measured at those locations. Noise-interferometry-based approximations to Green's functions can be used as the basis for a variety of inversion algorithms, thereby providing a purely passive alternative to active-source ocean acoustic remote sensing. In this paper we give an overview of results from noise interferometry experiments conducted in the Florida Straits at 100 m depth in December 2012, and at 600 m depth in September/October 2013. Under good conditions for noise interferometry, estimates of cross-correlation functions are shown to allow one to perform advanced phase-coherent signal processing techniques to perform waveform inversions, estimate currents by exploiting non-reciprocity, perform time-reversal/back-propagation calculations and investigate modal dispersion using time-warping techniques. Conditions which are favourable for noise interferometry are identified and discussed.

Key words: Interferometry; Wave propagation.

1 INTRODUCTION

Noise interferometry (NI) is the process by which an approximation to a Green's function, which describes propagation between two locations, is estimated by cross-correlating time series of ambient noise measured at those locations. The underlying theory (Rytov *et al.* 1989; Lobkis & Weaver 2001; Snieder 2004; Wapenaar 2004; Godin 2006, 2009; Garnier & Papanicolaou 2009; Boschi & Weemstra 2015) has been shown to be applicable to a wide variety of problems involving linear waves (Duvall *et al.* 1993; Rickett & Claerbout 2000; Haney 2009; Fricke *et al.* 2014; Godin *et al.* 2014a,b; Sabra *et al.* 2007a,b; Brown & Lu 2016). Seismic remote sensing applications have proven to be particularly successful (Campillo & Paul 2003; Shapiro *et al.* 2005; Yang *et al.* 2007; Gorbatov *et al.* 2013; Snieder & Larose 2013; Campillo & Roux 2014). Other commonly used names for NI include Green's function retrieval, ambient noise cross-correlation analysis and seismic coda cross-correlation analysis. In an underwater acoustic context, there have been many experimental demonstrations of the utility of the passive fathometer, which is a special case of NI that is designed to isolate bottom-reflected energy; in passive fathometry the two measurement locations are replaced by a single near-surface vertical line array and noise cross-correlations between all element pairs (including autocorrelations) are used in place of an isolated two-point cross-correlation (Siderius *et al.* 2006; Gerstoft *et al.* 2008; Siderius *et al.* 2010; Kim & Choi 2014; Yardim *et al.* 2014). Excluding that special geometry, relatively few experimental investigations of underwater acoustic NI have been reported (Roux *et al.* 2004; Fried *et al.* 2008; Brooks & Gerstoft 2009; Godin *et al.* 2010, 2014c; Lani *et al.* 2013; Sabra *et al.* 2013; Burov *et al.* 2014; Brown *et al.* 2014; Woolfe *et al.* 2015; Woolfe & Sabra 2015). In this paper, results of NI experiments conducted in December 2012 and September/October 2013 are reviewed. Some results from the first of those experiments are described in Brown *et al.* (2014), Godin *et al.* (2014c), Zang *et al.* (2015) and Godin *et al.* (2016). We emphasize throughout this paper that the information content of the noise cross-correlation functions (NCCFs) obtained using NI is comparable to that contained in measured responses to an active acoustic source.

The principal advantages of using underwater acoustic NI over active source remote sensing techniques (Munk *et al.* 1995) are that NI instrumentation: 1) requires very little power, 2) is compact and relatively easy to deploy and recover and 3) avoids possible harm (and associated legal and permitting issues) to marine mammals. The principal drawback associated with NI is that coherent stacking of many individual realizations of NCCFs—over some coherent

integration interval T_{ci}—must be performed to extract the coherent signal from the background incoherent energy contained in individual NCCFs. T_{ci} increases with increasing range, but array processing gain can be exploited to decrease T_{ci} (Sabra *et al.* 2005; Weaver & Lobkis 2005; Zabotin & Godin 2011). At longer ranges, ocean variability may prevent long-time coherent stacks from converging to stable/useful NCCFs. Also, in NI applications clock drifts can lead to a catastrophic loss of signal coherence between recording instruments. In contrast, in active source remote sensing applications, uncorrected clock drifts prevent one from obtaining accurate absolute travel time measurements, but that information loss need not be catastrophic. The limitations on NI imposed by ocean variability are currently not well known, which provides strong justification for performing experimental work of the type described here.

In this paper, we present the results of NI experiments conducted in the Straits of Florida in December 2012 at 100 m depth and in September/October 2013 at 600 m depth. In both experiments, the horizontal separations between instruments were 5, 10 and 15 km. Some results for the December 2012 experiment at 5 km and 10 km range are described elsewhere (Brown *et al.* 2014; Godin *et al.* 2014c, 2016; Zang *et al.* 2015) as noted where appropriate throughout this paper. The present paper differs in two important respects from those more specialized publications. First, we emphasize here self-consistency between different types of analysis, without repeating details that are described elsewhere. And second, we attempt here to give an objective overview and summary of results from both experiments, including some results at 15 km range (which have not previously been described), and including both positive results and disappointments (which have not previously been described). Our intention is to provide information on NI and passive ocean acoustic remote sensing that others will find useful in the design and execution of future NI experiments and in the interpretation of the data collected. In that spirit, knowledge of what doesn't work is as valuable as knowledge of what does work.

The remainder of this paper is organized as follows. In the following section the two experiments are briefly described, preliminary signal processing is briefly discussed, and NCCFs are presented. In Section 3, specialized wave-equation-based signal processing of the data to achieve specific goals is described. Both the December 2012 data set and the September/October 2013 data set are discussed, but emphasis is given to the former, reflecting the higher quality of that data set. Our results are summarized and discussed in Section 4. That section includes a somewhat speculative discussion of generally good and poor conditions for NI, and probable reasons that the December 2012 data was of higher quality than the September/October 2013 data.

2 EXPERIMENTAL WORK

The locations of the NI experiments conducted in the Straits of Florida in December 2012 and September/October 2013 are shown in Fig. 1. The same three instruments were deployed on short (7 m long) taut moorings in both experiments. Hydrophones were 5 m above the seafloor. In both experiments, the three instruments were deployed in a linear array with horizontal separations between instruments of approximately 5, 10 and 15 km. In both experiments, those linear arrays fell approximately on isobaths—at 100 m in December 2012, and at 600 m in September/October 2013. Sound speed profiles derived from CTD casts near instruments 1 and 3 are shown in Fig. 1 for both experiments. In both experiments, ambient noise in the frequency band of interest (20–80 Hz) was due predominantly to nearby weather-related sources (wind and associated wave-breaking) and shipping noise. Nearby weather buoys (http://140.90.238.27/station_page.php?station=MLRF1 and http://140.90.238.27/station_page.php?station=fwyf1) indicate that average surface wind speeds during both experiments were between 5.4 and 5.5 m s^{-1} with slightly higher variability during the December 2012 experiment (2.7 m s^{-1} standard deviation) than during the September/October 2013 experiment (2.1 m s^{-1} standard deviation). Shipping noise during both experiments was highly episodic, but with no obvious temporal characteristics distinguishing one experiment from the other. The spatial distribution of shipping noise sources may have been less homogeneous, on average, during the September/October 2013 experiment due to the closer proximity of that experiment to the port of Miami.

In both experiments described below, all three instruments were turned on in the laboratory and started recording approximately 2 d prior to deployment, and the instruments were turned off in the laboratory approximately 2 d after recovery. This was done to allow timing synchronization pulses to be transmitted simultaneously to all three instruments in the laboratory, both pre-deployment and post-recovery. The purpose of the timing synchronization pulses was to measure relative clock drifts, thereby allowing a linear clock drift correction (corresponding to a constant drift rate) between deployment and recovery to be applied. In addition, a month-long clock drift test was conducted in May of 2013 to assess the validity of the assumption that relative clock offsets grow very nearly linearly in time – and are therefore largely correctable. That test revealed relative clock drifts of approximately 1 ms d^{-1}, consistent with the manufacturers specifications, and that, over a one month period, deviations between actual clock time and the assumed linear offset correction were approximately 0.1 ms. These steps were taken to eliminate, to the extent possible, relative clock drifts because the associated coherence loss degrades NI-based estimates of Green's functions, which are constructed by coherently stacking many individual realizations of NCCFs.

The same instruments were deployed a third time in September/October of 2014. Following that experiment, all three instruments continued to run for a 6 d post-recovery clock drift test in the laboratory, during which three timing synchronization pulses were transmitted simultaneously to all three instruments. Analysis of the timing synchronization pulse data for that experiment revealed that between deployment and recovery relative clock drifts were as high a 7 ms d^{-1}, significantly higher than the manufacturers specifications for a new clock. Even more bothersome, relative clock drifts during the six day post-recovery test period differed significantly (including one difference in the sign of the relative drift) from the pre-deployment to post-recovery relative drift. We attribute this behaviour to loss of clock stability associated with aging. Consistent with these remarks, coherent stacking of short-time NCCF estimates in the September/October 2014 experiment did not result in any apparent noise reduction, or apparent convergence toward an approximation to a Green's function. The likely explanation for this behaviour is simple: over the coherent integration time interval required to produce stable NCCF estimates (several days to a week, we expect), coherence between instruments was lost at frequencies above about 10 Hz as a result of clock drifts (with relative clock errors of a few tens of ms). The September/October 2014 data will not be further discussed in this paper.

All of the NCCFs shown in this paper were constructed using the same procedure, which includes four important ingredients. First, short-time NCCFs were constructed using short blocks of data whose duration is $4 \times t_{\max}$, where $t_{\max}$ is slightly greater than

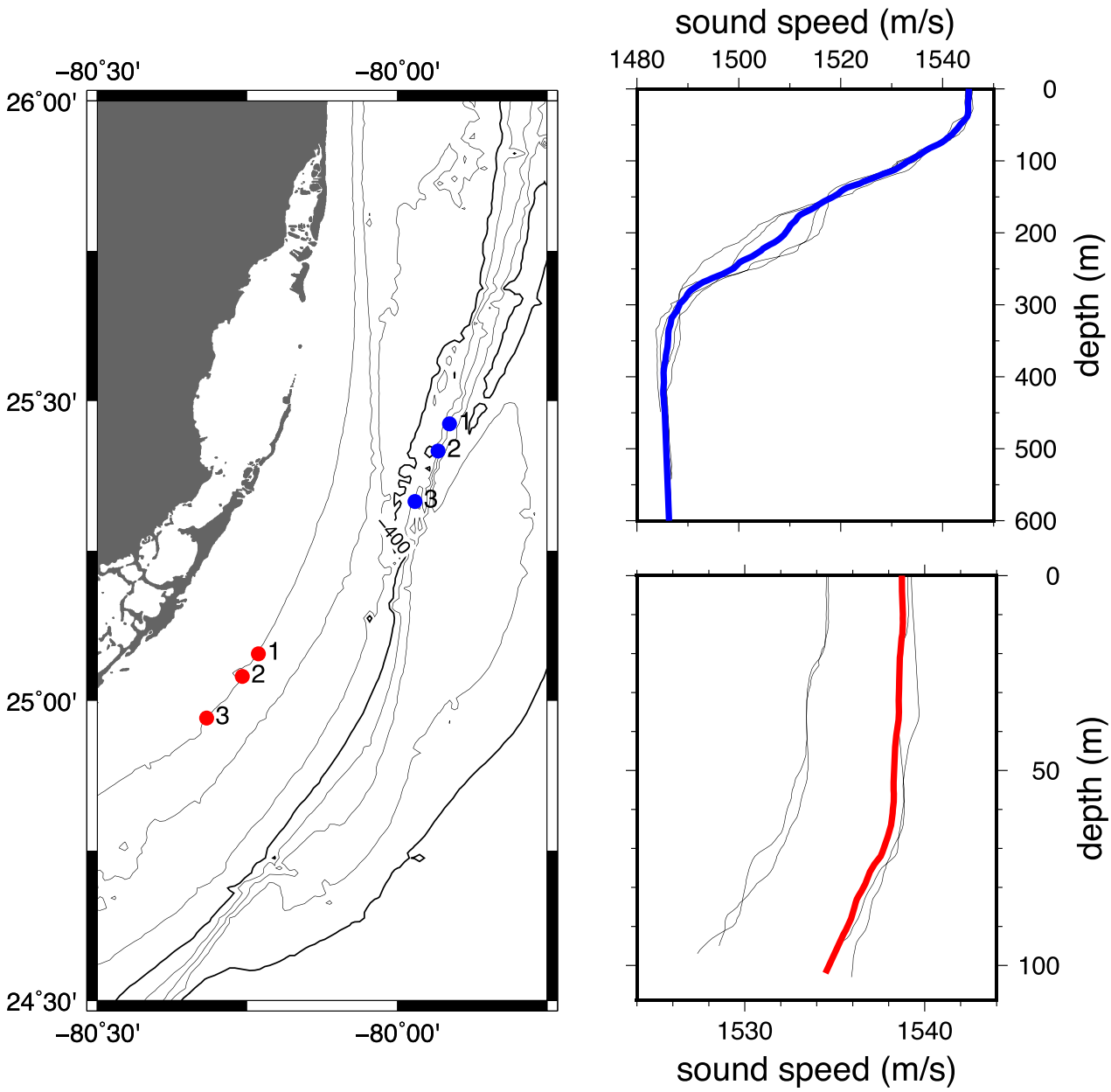

Figure 1. Left panel: map showing the positions of instruments 1, 2 and 3 in the December 2012 (red dots) and September/October 2013 (blue dots) NI experiments in the Florida Straits. The bathymetric contour interval is 100 m, with heavy lines at 400 and 800 m. Lower right panel: sound speed profiles (black lines) measured during the December 2012 deployment cruise and the February 2013 recovery cruise near instruments 1 and 3. The red curve is an estimate of the average sound speed profile during the 6 d measurement period. Upper right panel: sound speed profiles (black lines) measured during the September 2013 deployment cruise and the October 2013 recovery cruise near instruments 1 and 3. The blue curve is an estimate of the average sound speed profile during the 36 d measurement period. Note that the scales, both vertical and horizontal, are different in the upper and lower right panels.

the travel time of the last-arriving non-negligible energy connecting the relevant instrument pair. (This choice allows NCCFs to be constructed in the frequency domain with temporal lags between $-t_{max}$ and $+t_{max}$ while avoiding wrap-around effects.) Second, the spectra of those short-time NCCFs were whitened over the frequency band chosen. Third, all short-time NCCFs were normalized to have the same maximum amplitude. And fourth, all short-time NCCFs within a much longer time window were coherently added to slowly build up the signal-to-noise ratio (SNR). (Here and below, SNR is based on the ratio of coherent energy to incoherent energy; for 'noisy' NCCFs this ratio is small.) No data were discarded; the aforementioned normalization prevents spurious events like a nearby passing ship from overwhelming the long-time NCCF estimate. The procedure just described is slightly different from the procedure used in Brown *et al.* (2014) and Godin *et al.* (2014c); NCCFs computed using the two techniques are almost identical. The point here is not that one technique is better than the other; rather, we emphasize that the NCCFs presented here are quite robust.

2.1 The December 2012 experiment

NCCFs constructed from the ambient noise data collected during the December 2012 experiment are shown in Figs 2 (1–2 instrument

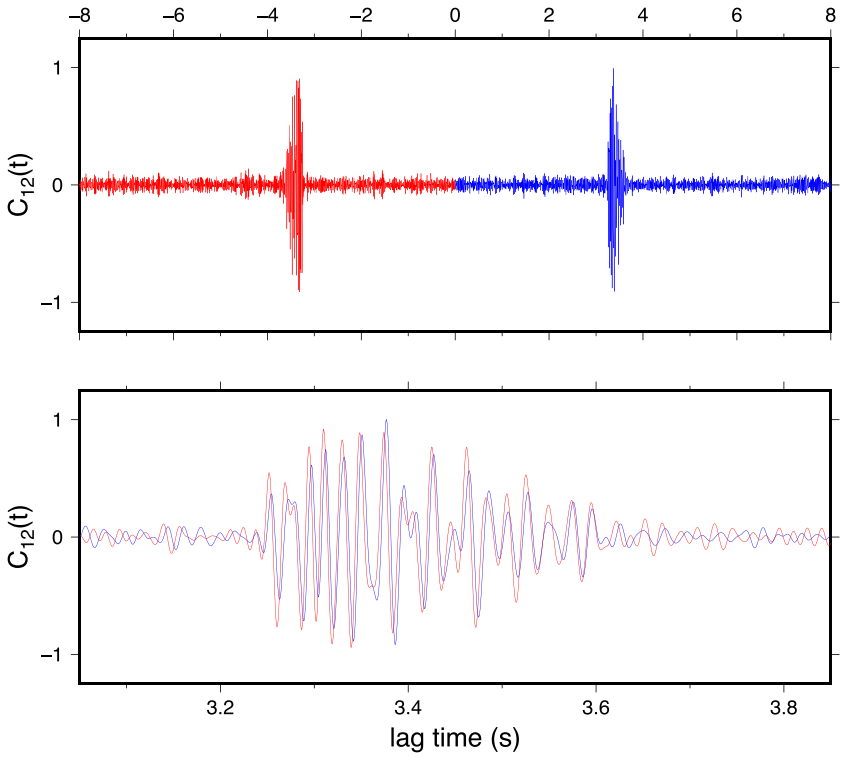

Figure 2. Upper panel: 1–2 instrument pair NCCF in the 20–70 Hz band, corresponding to a 6 d coherent average, for the December 2012 experiment. Lower panel: blow up of the energetic signal portion of the NCCF, with positive and negative lag structure superimposed. Red and blue curves correspond to negative and positive lags, respectively.

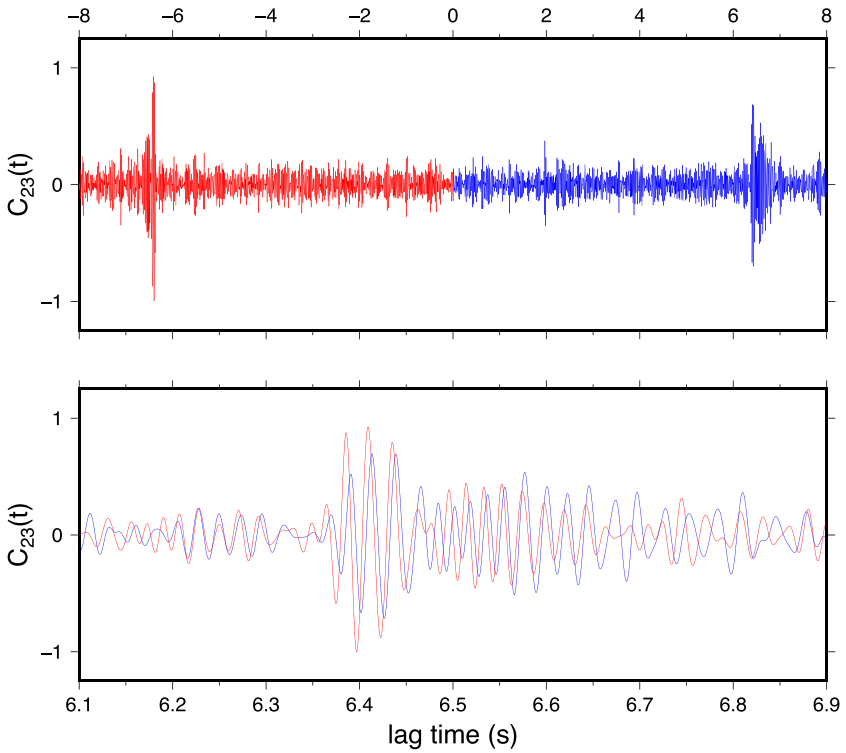

Figure 3. Upper panel: 2–3 instrument pair NCCF in the 20–70 Hz band, corresponding to a 6 d coherent average, for the December 2012 experiment. Lower panel: blow up of the energetic signal portion of the NCCF, with positive and negative lag structure superimposed. Red and blue curves correspond to negative and positive lags, respectively.

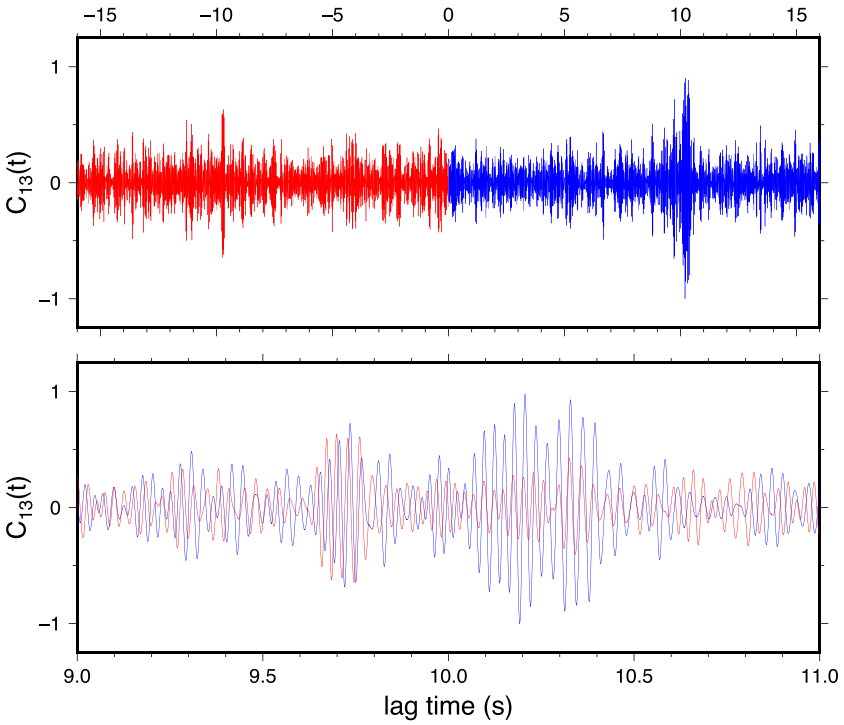

Figure 4. Upper panel: 1–3 instrument pair NCCF in the 20–50 Hz band, corresponding to a 6 d coherent average, for the December 2012 experiment. Lower panel: blow up of the energetic signal portion of the NCCF, with positive and negative lag structure superimposed. Red and blue curves correspond to negative and positive lags, respectively.

pair, 5 km separation), 3 (2–3 instrument pair, 10 km separation) and 4 (1–3 instrument pair, 15 km separation). In all cases the coherent integration time T_{ci} was approximately 6 d. Convergence of the 1–2 instrument pair NCCF toward the relatively high SNR structure seen in Fig. 2 is discussed briefly in Brown *et al.* (2014) and Godin *et al.* (2014c). SNR is clearly highest for the 1–2 instrument pair and lowest for the 1–3 instrument pair, which is consistent with the expectation that the required coherent integration time increases with increasing range. The NCCF shown in Fig. 4, corresponding to the 1–3 instrument pair is clearly very noisy. In spite of that, we show in Sections 3.2 and 3.4 that that NCCF contains useful information about the environment that is entirely consistent with the information contained in the NCCFs corresponding to the 1–2 and 2–3 instrument pairs. Brown *et al.* (2014) and Godin *et al.* (2014c) include figures showing shorter duration NCCFs for the 1–2 instrument pair that reveal (1) convergence toward a stable NCCF and (2) short-term variability associated with time-dependence of the noise sources.

None of the three figures (Figs 4–6) showing NCCFs reveal any temporally resolved arrivals that can be identified with isolated rays; ray simulations predict many rays connecting all three instrument pairs with travel times falling inside the energetic portions (at both positive and negative lag) of the NCCFs. Predicted ray travel times are not shown in the figures, both because of the absence of temporally resolved ray arrivals in the NCCFs and because the ray approximation is of questionable validity in this environment in the relevant frequency band, 20–70 Hz. On the other hand, the modal description of the wave field is both valid and useful, and is exploited in Sections 3.1, 3.3 and 3.4.

After approximately 6 d of continuous, simultaneous and uninterrupted data recording by all three instruments, gaps in instrument 2 data started to appear. Instruments 1 and 3 behaved similarly starting at later times. This behaviour limited the time window over which uninterrupted simultaneous ambient noise measurements were made on all three instruments to 6 d. In addition to losing ambient noise data, the post-recovery timing synchronization pulse was not recovered on any of the instruments. To compensate for the latter loss, a boot-strapping method, which is described in Godin *et al.* (2014c), was employed to recover relative clock drifts. That analysis assumed that relative clock offsets grow linearly in time, that is, the relative drift rates are constant. (Recall that the same assumption is made when the timing synchronization pulses are used to estimate drift rates.) Also, it was assumed that the current-induced timing shift (see Section 3.2) was constant over the six-day measurement period. Using 1.5 d NCCFs a linear regression analysis of both 1–2 and 2–3 timing shifts was performed over the six day measurement period. That analysis provided estimates of the constant drift rates, Δ_{12} and Δ_{23}, and the associated current-induced timing shifts. We emphasize here the consistency of those results. First, the two associated depth-averaged current estimates are very close (approximately 0.5 m s^{-1} in the northward direction). Second, because $\Delta_{13} = \Delta_{12} + \Delta_{23}$, the 1–3 instrument pair 6 d NCCF (shown in Fig. 4) provides an additional means to check for consistency. In this regard, we note here that without applying the $\Delta_{13} = \Delta_{12} + \Delta_{23}$ correction when processing the 1–3 ambient noise data, no useful NCCF could be produced. With that drift correction, the NCCF shown in Fig. 4 was produced.

2.2 The September/October 2013 experiment

In the September/October 2013 experiment, approximately 36 d of data were recorded. Additionally, both the pre-deployment and post-recovery timing synchronization pulses were recovered. The timing synchronization data resulted in relative clock drift corrections of approximately 1 ms d^{-1}, consistent with the manufacturers

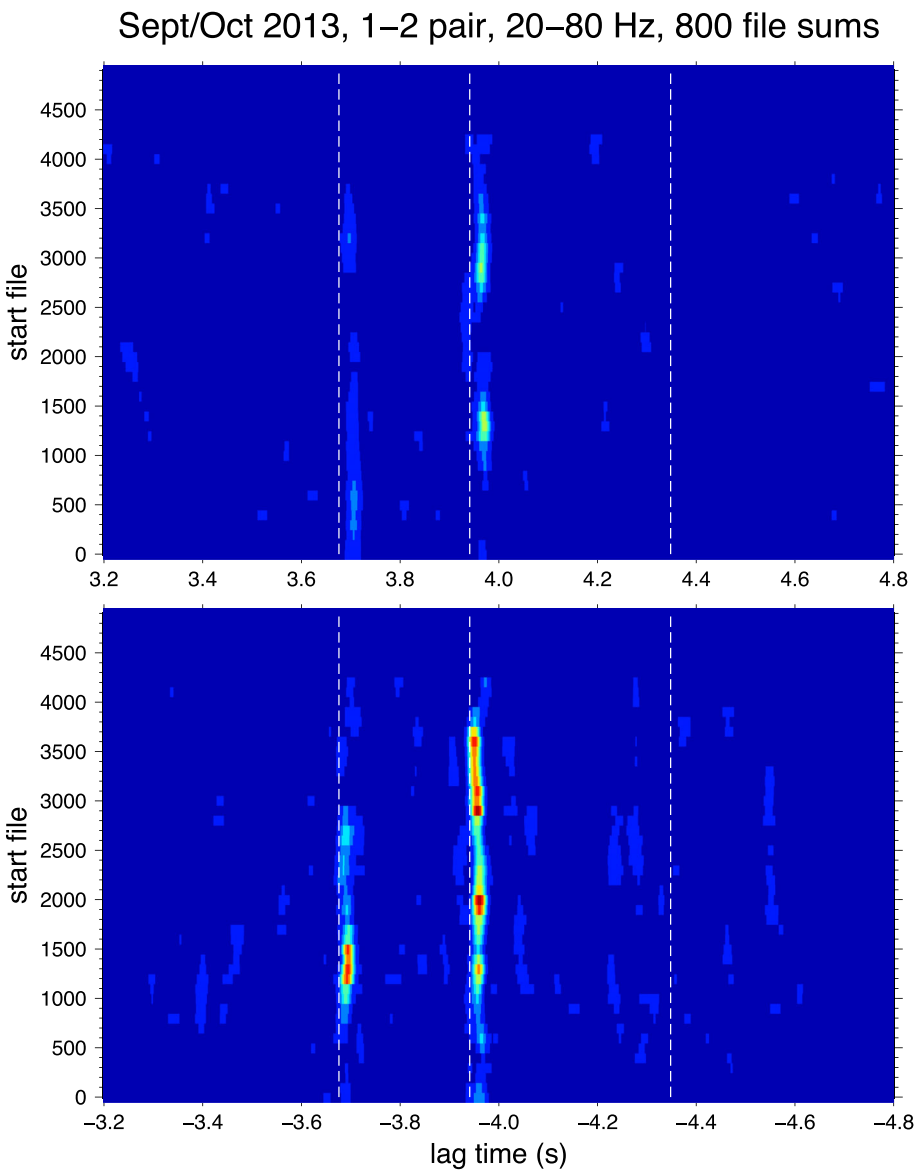

Figure 5. NCCF intensity versus lag for the 1–2 instrument pair throughout the duration of the September/October 2013 experiment. The upper and lower panels correspond to positive and negative lag, respectively. Each intensity versus lag horizontal stripe of the figure was computed by coherent integration over 800 successive files, with the first file in each 800-file block staggered by 100 files. 800 files extend over a period of 5.79 d; equivalently 100 files correspond to 0.72 d. The seven final (uppermost) intensity versus lag horizontal stripes in each plot are based on processing fewer (700, 600, 500, . . . 100) than 800 successive files. NCCF intensity was computed as the squared envelope of the NCCF waveform. Intensity was normalized to lie between 0 and 1 for the pair (positive and negative lag) of plots shown; the colour bar is based on a linear intensity scale where 0/1 is mapped onto dark blue/red. The vertical dashed white lines show the predicted arrival times of three ray arrivals.

specifications; linear drift corrections were applied. The longer data set allowed for more data processing flexibility than was possible with the 6 d of uninterrupted data collected during the December 2012 experiment. In particular, the coherent stacking time T_{ci} could be as long as 36 d using the September/October 2013 data. Unfortunately, exploration of T_{ci} revealed that increasing T_{ci} beyond about one week did not result in better (with apparently higher SNR) NCCFs. We attribute this behaviour to a combination of coherence loss resulting from ocean variability and disadvantageous NI conditions associated with the downward refracting sound speed profile; recall Fig. 1. The latter point is discussed in the final section. (Coherence loss associated with a nonlinear clock drift that we have not accounted for is another possible contributing factor, but we are aware of no reason to suspect that the linear drift correction that was applied was inadequate.)

De-phased NCCFs constructed from the ambient noise data collected during the September/October 2013 experiment are shown in Figs 5 (1–2 instrument pair, 5 km separation) and 6 (2–3 instrument pair, 10 km separation). Phase information is removed in those plots to highlight the gross structure of the time-evolving NCCFs. The NCCFs shown in Figs 5 and 6 were constructed as coherent stacks over approximately 5.79 d (800 data files) of short-time NCCF estimates, with the start time staggered by 0.72 d (100 data files). In those plots file number 0 is taken to correspond to the first set of post-deployment data files that was recorded on all three instruments. Plots similar to Figs 5 and 6 have been produced

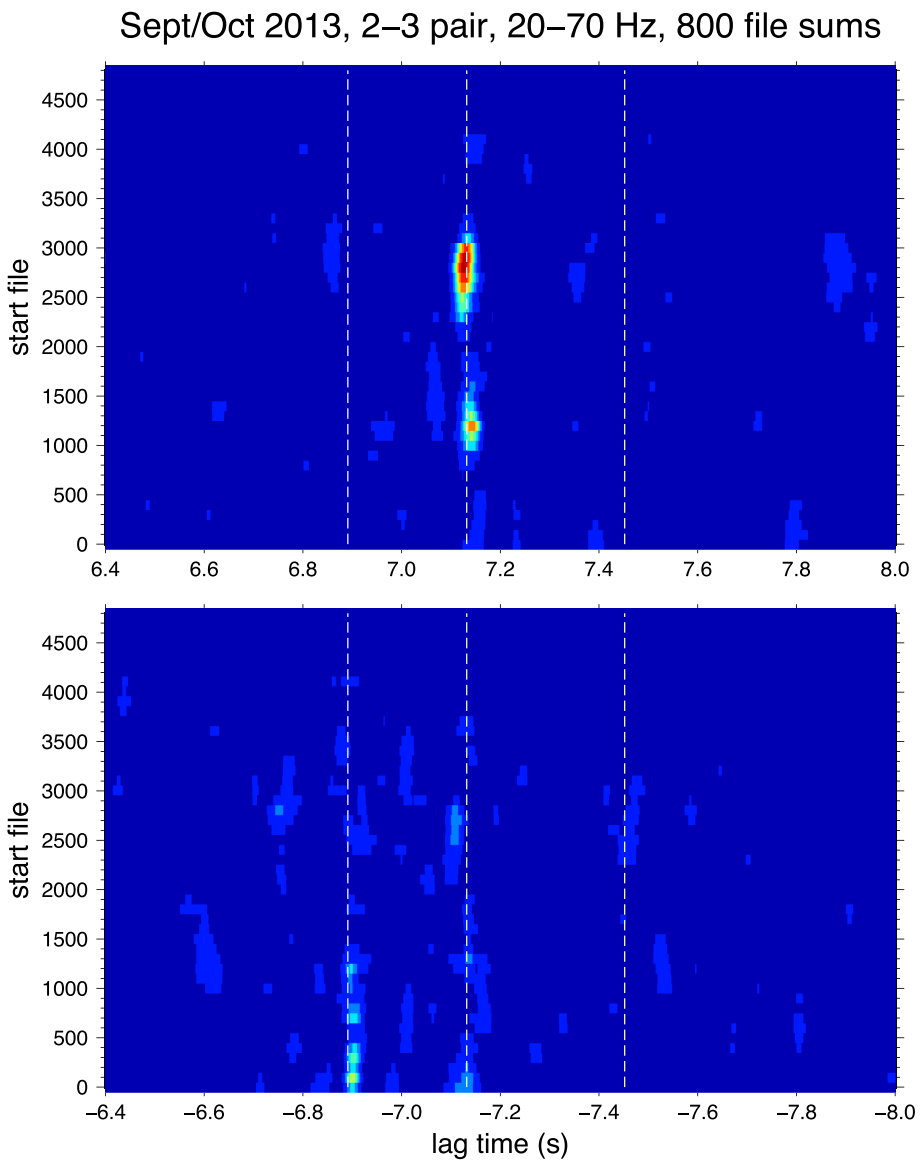

Figure 6. Same as Fig. 5, but for the 2–3 instrument pair.

using different coherent integration times, both shorter and longer, and using different bandwidths, but in no case have we observed results that are clearly superior to Figs 5 and 6. Unfortunately, the September/October 2013 data appear to be of lower quality than the December 2012 data.

This statement is supported by Fig. 7 which shows one of the better examples of an NCCF, including phase information, that has been produced using the September/October 2013 experimental data. Like in Figs 5 and 6, the coherent integration time was 5.79 d. The data quality is not awful, but is clearly inferior to the December 2012 NCCF shown in Fig. 2, at approximately the same range and with approximately the same coherent integration time.

Although the NCCFs from the December 2012 experiment are generally of higher quality than those from the September/October 2013 experiment, the latter set of NCCFs are simpler to interpret inasmuch as a small number of ray arrivals are temporally resolved. The travel times of predicted ray arrivals are shown in Figs 5–7 and are seen to be in generally good agreement with the onset of what appears to be energetic temporally resolved ray arrivals in the NCCFs. (In all cases the ray is actually a cluster of four rays that are up/down-going at receiver *A* and up/down-going at receiver *B*. Because all receivers are 5 m above the seafloor, these four rays have nearly equal travel times. The plotted travel time is, in each case, the travel time of the first arrival in the cluster of four ray arrivals.) In Figs 5–7, early/late arrivals correspond to flatter/steeper rays. It is useful to keep in mind that the energy in NCCFs is due primarily to strongly excited energy following rays that pass through both receivers. The relevant contributing noise sources are thus predominantly sources that lie in the vertical plane passing through both receivers. Moreover, the ray angle cannot be too flat because flat angle energy is only weakly excited by near-surface noise sources (which excite energy with a radiation pattern approximately consistent with vertically oriented dipoles because of the pressure-release boundary condition at the surface). Also, if the ray angle is too steep (steeper than the bottom critical angle) bottom reflection loss will be substantial. These comments lead us to expect that the strongest arrival should have some intermediate ray angle. Unfortunately, the quality and stability NCCFs shown in Figs 5 and 6 are too poor to allow us to try to quantify these amplitude versus ray angle trends.

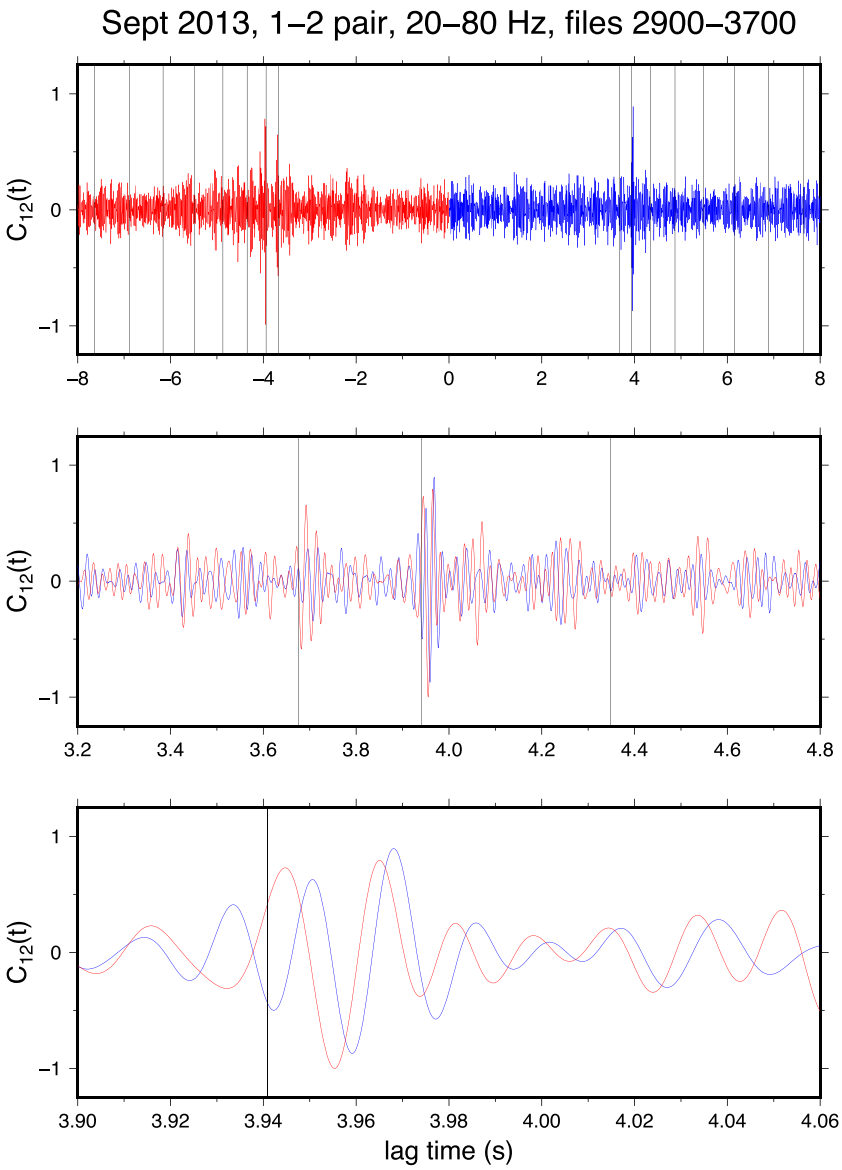

Figure 7. Upper panel: 1–2 instrument pair NCCF in the 20–80 Hz band, corresponding to a 6 d coherent average, for the September/October 2013 experiment. The 6 d time period corresponds to files 2900 to 3600 on Fig. 5. Lower two panels: blow up of the energetic signal portion of the NCCF, with positive and negative lag structure superimposed. Red and blue curves correspond to negative and positive lags, respectively. The vertical black lines on all three plots correspond to predicted ray arrival times.

3 RESULTS

In the four subsections that follow, we give an overview of results relating to four types of analysis that have been performed using the two data sets described above.

3.1 Waveform modelling and inversion

A basic form of phase-coherent signal processing to perform using a measured NCCF is numerical simulation of the NCCF using wave-equation-based methods. The fundamental result underlying NI is (Rytov *et al.* 1989; Lobkis & Weaver 2001; Snieder 2004; Wapenaar 2004; Godin 2006, 2009; Garnier & Papanicolaou 2009; Zang *et al.* 2015)

$$\frac{\mathrm{d}}{\mathrm{d}t}C_{AB}(t) \approx D(t) * [G_{BA}(-t) - G_{AB}(t)]. \quad (1)$$

Here $G_{AB}(t)$ is the transient Green's function for acoustic pressure at location B corresponding to a point source at location A and similarly for $G_{BA}(t)$, $*$ denotes convolution, $D(t)$ is a band-limited approximation to a delta function, and $C_{AB}(t) = \int p_A(\tau)p_B(\tau + t)\,\mathrm{d}\tau$ is the cross-correlation function of acoustic pressure measurements at locations A and B. Note that we have defined $C_{AB}(t)$ such that the positive lag ($t > 0$) structure corresponds to propagation from A to B, and the negative lag structure corresponds to propagation from B to A. This distinction is important if reciprocity is violated due to the presence of background currents, in which case $G_{AB}(t) \neq G_{BA}(t)$. The simplest physical interpretation of the acoustic pressure Green's function is the response to a source of mass q (with units kg m^{-3} s^{-1}) for which $\partial q/\partial t$ is proportional to $\delta(t)\delta(\mathbf{x})$. If the acoustic pressure measured a short distance from an acoustic point source at location i has time history $s_i(t)$, the acoustic pressure at a distant location is $s_i(t)$ convolved with the appropriate acoustic pressure Green's function. The critical assumptions underlying eq. (1)

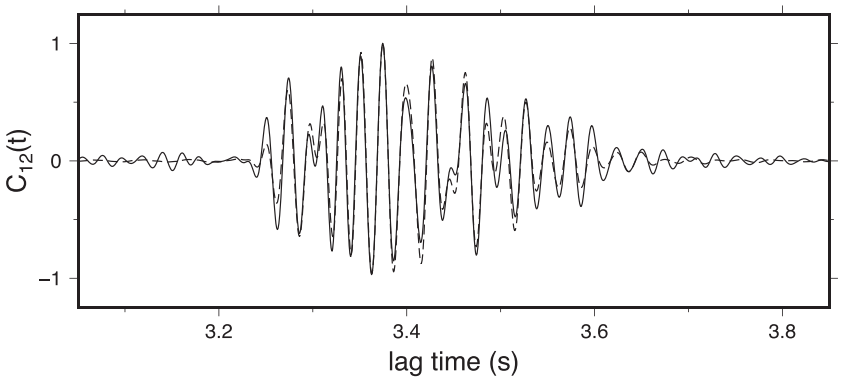

Figure 8. A comparison of measured (solid line) and simulated (dashed line) NCCFs in the 20–70 Hz band. The spectral window applied to both NCCFs is a Hann window whose zeros are at 20 and 70 Hz, so the effective bandwidth is less than 50 Hz. Both NCCFs were normalized to have the same maximum amplitude. The simulated NCCF was computed using the optimal eight-parameter model described in the text.

are (1) the distribution of sources is approximately diffuse and (2) $s_i(t)*s_j(-t) = \delta_{ij}D(t)$. These assumptions are only approximately satisfied in typical ocean conditions. In spite of that, eq. (1) remains a very good approximation provided the distribution of noise sources is approximately diffuse, and the Green's functions in that equation are interpreted as weighted Green's functions where the weighting is controlled by the angular dependence of the ambient noise field.

Waveform modelling of $C_{AB}(t)$ based on eq. (1) is described in Zang *et al.* (2015). That analysis focuses on the 1–2 instrument pair NCCF computed using the December 2012 experimental data (because those were the experimental NCCFs with the highest SNR). In that work current-induced timing shifts ($+\delta t$ at positive lag and $-\delta t$ at negative lag, as described below) were removed, and then, to slightly increase SNR, the positive and negative lag portions of the NCCFs were added. Constructing a wave-equation-based prediction of an NCCF is closely related to calculating the corresponding Green's function, but care must be taken to account for the small differences, consistent with eq. (1), between $C_{AB}(t)$ and $G_{AB}(t)$, in addition to the angular weighting of the Green's function. The weighting function employed in that work consisted of a product of two terms: a term that accounts for the predominance of near-surface sources and the associated vertical dipole radiation pattern (because of the pressure-release boundary condition at the sea surface), and a term that accounts for the fact that coherent averaging over an interval longer than a tidal cycle effectively filters out steep angle energy at higher frequencies (see Zang *et al.* 2015 for details). The principal complication associated with waveform modelling of $C_{AB}(t)$ is the fact that $G_{AB}(t)$ (weighted or not) depends on the environment which is known only approximately. (The water column sound speed structure was measured, but geoacoustic properties were not.) With this in mind, the inverse problem was treated in Zang *et al.* (2015) as an integral part of the process of comparing measured and simulated NCCF waveforms. In that work simulations were performed using the KRAKEN normal mode model (Porter 1997). In the associated inversion, the environment was parameterized using a stratified model consisting of a homogeneous ocean with a flat bottom, and a lossy fluid sediment layer overlying a substrate. The model included eight free parameters: the sediment layer sound speed, thickness, density and attenuation; the substrate sound speed, density and attenuation; and the range between instruments. (Consistent with O(10 m) positioning uncertainty of our instruments, range was treated as an adjustable parameter.) We refer to the resulting best-fitting model as the optimal eight-parameter model.

Measured and simulated (using the optimal 8-parameter model) NCCFs in the 20–70 Hz band are shown in Fig. 8. Agreement is excellent; the energetic portions of the normalized NCCFs, between 3.2 and 3.7 s, have a correlation coefficient of 0.963. The conclusion to be drawn from Fig. 8—and, more generally, the results in Zang *et al.* (2015)—is that wave-equation-based waveform modelling and inversion using measured NCCFs is feasible. A comparison of measured and simulated NCCFs in multiple overlapping narrow bands will be considered and further explored in Section 3.4. An advantage of displaying NCCFs in multiple overlapping narrow frequency bands is that such a time-frequency plot provides a natural way to display and investigate modal dispersion.

3.2 Estimation of currents

As described in Section 3.1, measured ambient noise NCCFs contain information about propagation in both directions between sensors. Specifically, the positive lag portion of the C_{AB} NCCF describes propagation from A-to-B, while the negative lag portion describes propagation from B-to-A. The significance of A-to-B versus B-to-A propagation is that in the presence of background currents, reciprocity is violated, and the difference between the positive and negative lag structure of C_{AB} can be used to estimate the component of current in the vertical plane connecting A and B. For propagation with/against a horizontal current in a nearly homogeneous ocean, the current-induced travel time perturbation is approximately $\delta T \approx \mp ru/c^2$, where r is range, c is sound speed, and, if the sound makes many surface and bottom reflections, u is the depth-averaged current speed.

This idea was exploited in Godin *et al.* (2014c) to estimate the depth averaged current between the 1–2 and 2–3 instrument pairs in the December 2012 experiment. As noted above, in that analysis the measured 1–2 and 2–3 NCCFs were used to estimate both the 1–2 and 2–3 relative clock drifts, Δ_{12} and Δ_{23}, and the depth-averaged current along the 1–2 and 2–3 paths. NCCFs for the 1–3 instrument pair were not used in that analysis because without application of any Δ_{13} clock drift correction, it was not possible to construct a useful (with positive SNR) NCCF for the 1–3 instrument pair. But Fig. 4 shows that after applying the $\Delta_{13} = \Delta_{12} + \Delta_{23}$ clock correction, a useful, albeit with low SNR, NCCF for the 1-3 pair can be produced. We demonstrate in Section 4 that the energy between lags 9.5 and 9.8 s corresponds to mode 1, and that energy between lags 9.8 and 10.5 s corresponds to mode 2. Evidently (see Fig. 4), mode 2 energy is more strongly excited in the 1-to-3 direction than

in the 3-to-1 direction; this is presumably due to inhomogeneity of noise sources. The time shift between positive and negative lag of the mode 1 energy (with relatively high SNR) in Fig. 4 is $2\delta T = 3.8$ ms, corresponding to $u = 0.59$ m s^{-1} in the 3-to-1 direction. This estimate is close to the estimate of 0.47 m s^{-1} in the 3-to-1 direction reported in Godin *et al.* (2014c).

Similarly, in Fig. 7, corresponding to the September/October 2013 experiment, the difference in travel time at positive and negative lags ($2\delta T$) of the ray arrival between approximately 3.94 and 3.99 s is about 2 ms. (Because the energetic portions of the waveforms at positive and negative do not match very well, we intentionally specify this number with only one significant digit.) This corresponds to a depth-averaged (in this case with non-uniform depth weighting due to the corresponding ray path geometry) current estimate of approximately 0.5 m s^{-1} in the south-to-north direction. Both the sign and magnitude of this estimate are consistent with the instrument array being approximately aligned, in the 3-to-1 direction, with the Florida Current. Unfortunately, as shown in Fig. 5, the stability of the NCCFs throughout the duration of this experiment was disappointingly low, providing little incentive to further pursue the investigation of NI-based current estimation using the September/October 2013 data set.

3.3 Time-reversal/back-propagation simulations

It is now widely appreciated (Jackson & Dowling 1991; Fink *et al.* 2000; Edelman *et al.* 2002; Kuperman *et al.* 2010) that if a transient signal is generated at one point and the resulting field is recorded at multiple distant locations, then retransmitting the time-reversed recorded signals at those locations results in a wave field that focuses at the original sound generation point. This process is referred to as implementation of a time reversal mirror (TRM). It was first demonstrated by Roux & Kuperman (2005) that NCCFs, rather than measured responses to active source transmissions, can be used to successfully implement a TRM; using NCCFs one of the receivers acts as a virtual source, while the other acts as a virtual receiver. In Godin *et al.* (2016), it is shown that NCCFs from the December 2012 NI experiment described above can be used to implement a TRM, and that by searching over a suitable model parameter space to find the model that optimally focuses the back-propagated energy at the position of the virtual source, this combination of signal processing techniques can be used to address the inverse problem.

Before commenting further on the inverse problem, it is important to note an important difference between the TRMs implemented in Roux & Kuperman (2005) and Godin *et al.* (2016). In general, path diversity is essential to produce a good back-propagation focus when implementing a TRM; in the ideal case the transmitted signal is measured at all locations, time-reversed and retransmitted. In Roux & Kuperman (2005) NCCFs were computed for many pairs of receivers on different vertical line arrays at mid-depth in the deep ocean; diversity was achieved because for each virtual source there were many virtual receivers. In contrast, in Godin *et al.* (2016) diversity was achieved because of the multitude of ray paths connecting one virtual source and one virtual receiver.

The inverse analysis presented in Godin *et al.* (2016) used a model that was qualitatively similar to the eight-parameter model described above, but with only four parameters (sediment sound speed, sediment density, sediment thickness and substrate sound speed); that analysis resulted in an optimal estimate of the environment consistent with the assumed parametrization. One cannot expect complete agreement between the TRM-based inversion results presented in Godin *et al.* (2016) and the NCCF waveform-modelling-based inversion work (Zang *et al.* 2015) for several reasons: (1) differences in model parametrizations; (2) different measures of optimality were used in the two studies; and 3) the TRM-based work was based on wide-angle parabolic equation calculations, while the waveform-modelling work was based on a Helmholtz-equation-based calculations. In spite of these differences, if both analyses are essentially correct (they are), one expects that if a TRM is implemented using the optimal eight-parameter environment and using a Helmholtz-equation-based wave field calculation, a sharp focus should be produced in the back-propagated field at the correct position of the virtual source. This is indeed the case, as illustrated in Fig. 9. In

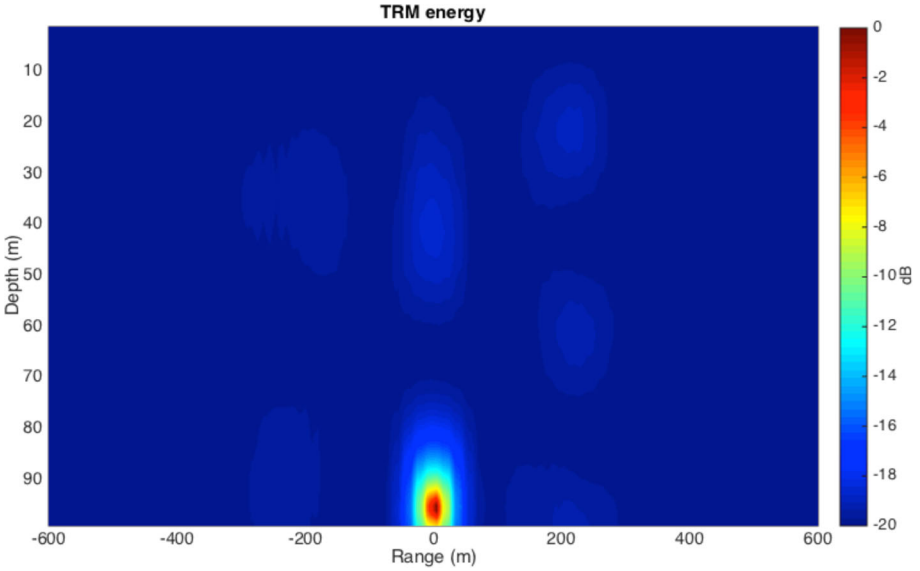

Figure 9. The result of implementing a TRM using the 1–2 instrument pair NCCF from the December 2012 NI experiment. Integrated energy of the back-propagated wave field in the interval -0.03 s $< t < 0.03$ s is shown as a function of position near the virtual source. The main focal peak is displaced from the estimated position of the virtual source by about 2 m. Focal side lobes are approximately 16 dB below the main peak. In this environment, focal side lobes in the back-propagated wave field are small as a result of many multipaths contributing to the NCCF.

fact, the optimal eight-parameter model produces a sharper virtual source focus than the optimal four-parameter model. Fig. 9 illustrates several points: (1) consistency between the analyses described in Zang *et al.* (2015) and Godin *et al.* (2016), (2) demonstration that a TRM can be implemented with only one virtual source and one virtual receiver owing to the significant path diversity in this environment and (3) demonstration that NCCFs can be used to perform advanced phase-coherent wave-equation-based signal processing techniques.

3.4 Investigating modal dispersion using time-warping techniques

In this subsection, we present results of applying a signal processing technique, referred to as time-warping, to NCCFs constructed using the December 2012 ambient noise data. The purpose of this type of processing is to isolate one or more modal pulses (broad-band distributions of energy corresponding to fixed mode numbers). Recall that traditional (linear-theory-based) approaches to mode-filtering require that measurements be made at many locations to exploit orthogonality of the modes. In contrast, time-warping is based on the premise that if the (generally nonlinear) time-dependence of a modal pulse is known in an environment close to the measurement environment, then, by making use of an appropriately stretched (or 'warped') time coordinate, that modal pulse can be isolated by appropriately processing a wave field time history measured at an isolated location. Time-warping is a nonlinear phase-coherent signal processing technique. Here we apply time-warping to measured NCCFs both to demonstrate the feasibility of applying this advanced signal processing technique to ambient-noise-based data, and to demonstrate that the results are consistent with the results presented in Sections 3.1 and 3.3.

The time-warping transformation used here has previously been applied to active transmission acoustic data collected in shallow-water waveguides (Bonnel *et al.* 2010, 2013; Bonnel & Chapman 2011). That transformation is exact in an ideal (range-independent, homogeneous ocean, rigid bottom) shallow water waveguide, but those references show that the transformation is quite robust in that it works well in real shallow water waveguides. A detailed time-warping analysis of the December 2012 Florida Straits NI data, with the objective of quantifying effective attenuation associated with coherence loss, will be described elsewhere.

Here we implement the time-warping transformation in a way that retains phase information, thereby allowing us to compare measured and simulated modal pulse waveforms. The motivation for performing this analysis is illustrated in the upper panels of Figs 10–12. Those figures show a comparison of measured and simulated NCCFs in overlapping 10 Hz bands for the 1–2, 2–3 and 1–3 instrument pairs, respectively, in the December 2012 NI experiment, with predicted dispersion curves for the same 10 Hz bands superimposed. (The predicted dispersion curves and simulated NCCFs were computed using the optimal eight-parameter model described above. The spectral weighting function applied in each 10 Hz band is a Hann window, whose zeros are at $f_0 \pm 5$ Hz, so the effective bandwidth is actually less than 10 Hz. The width of modal pulses is predicted to extend beyond the dispersion curve limits shown, as a result of diffractive smearing (Brown *et al.* 1996; Udovydchenkov & Brown 2008).) To assess to correctness of the predicted dispersion characteristics shown in those figures, it is necessary to isolate the contributions to those wave fields from individual modal pulses. To achieve that goal, we make use of time-warping.

Time-warping, as implemented here, is done in five steps. First, each broad-band NCCF is resampled uniformly in warped time $t' = \sqrt{t^2 - t_{\rm ref}^2}$ where $t_{\rm ref}$ is the signal start time. We used $t_{\rm ref} =$ 3.251, 6.356 and 9.607 s for the 1–2, 2–3 and 1–3 instrument pairs, respectively, in the results shown; those results are not sensitive to small variations in the choice of $t_{\rm ref}$. Second, spectra are computed in the warped domain. The time-warping transformation leads to a downshift of frequencies in the warped domain. More importantly, spectra in the warped domain reveal that contributions from different mode numbers have very narrow spectral signatures that drift very little in warped time, and are isolated from each other. With these properties in mind, the third step is to band-pass filter the time-warped broad-band signal to isolate the contribution from individual mode numbers, that is, to isolate individual modal pulses. Step four is to transform each modal pulse back to the original time domain, $t = \sqrt{t'^2 + t_{\rm ref}^2}$. Finally, in step five, each broad-band modal pulse in the unwarped t-domain is passed through a bank of overlapping narrow band-pass filters to help reveal dispersion of energy associated with the corresponding mode number.

Results are shown in Figs 10–12. For the 1–2 instrument pair (5.00 km range, Fig. 10) contributions from the first four modes are isolated at centre frequencies f_0 of 25, 30, 35 ... 75 Hz. For the 2–3 instrument pair (9.78 km range, Fig. 11) contributions from the first two modes are isolated at centre frequencies f_0 of 25, 30, 35 ... 65 Hz. For the 1–3 instrument pair (14.78 km range, Fig. 12) contributions from the first two modes are isolated at centre frequencies f_0 of 25, 30, 35, 40 and 45 Hz. The approximate upper limits on frequency and mode number in these plots are imposed by the signal processing that we have performed; the combination of tidal fluctuations of water depth and the coherent stacking of short-time NCCFs result in the effective attenuation of steep-angle (higher mode number) energy, especially at higher frequencies and longer range (Brown *et al.* 2014). Agreement between data-based and simulation-based estimates of narrow-band modal pulses is generally good, with generally better agreement for the 1–2 instrument pair than for the 2–3 and 1–3 instrument pairs. This is not primarily a signal-to-noise issue. Instead, we think that the principal reason that agreement is better for the 1–2 pair is that the assumed environmental model was optimized for the measured 1–2 NCCFs. In this context we note that measured bathymetric variations between the 1–2 instrument pairs were between 97 and 101 m, while those between the 2–3 instrument pairs were between 86 and 100 m. To compute simulated NCCFs between the 1–2 instrument pairs the environment was assumed to be range-independent, while measured bathymetric variations between the 2–3 and 1–3 instrument pairs were accounted for using an adiabatic mode approximation. Also note that, as expected (Brown *et al.* 1996; Udovydchenkov & Brown 2008), the temporal separation between modal pulses increases with increasing range.

4 CONCLUSIONS AND DISCUSSION

Although the theoretical foundation for NI is now firmly established, many questions relating to the limitations of NI require experimental investigation. This is particularly true in an ocean acoustic context. Among the questions that need to be answered are the following. What limitations on NI are imposed by ocean fluctuations? What limitations on NI are imposed by a non-diffuse distribution of noise sources, especially shipping noise? Can anisotropy of the ambient noise field be predicted and accounted for? Which environmental

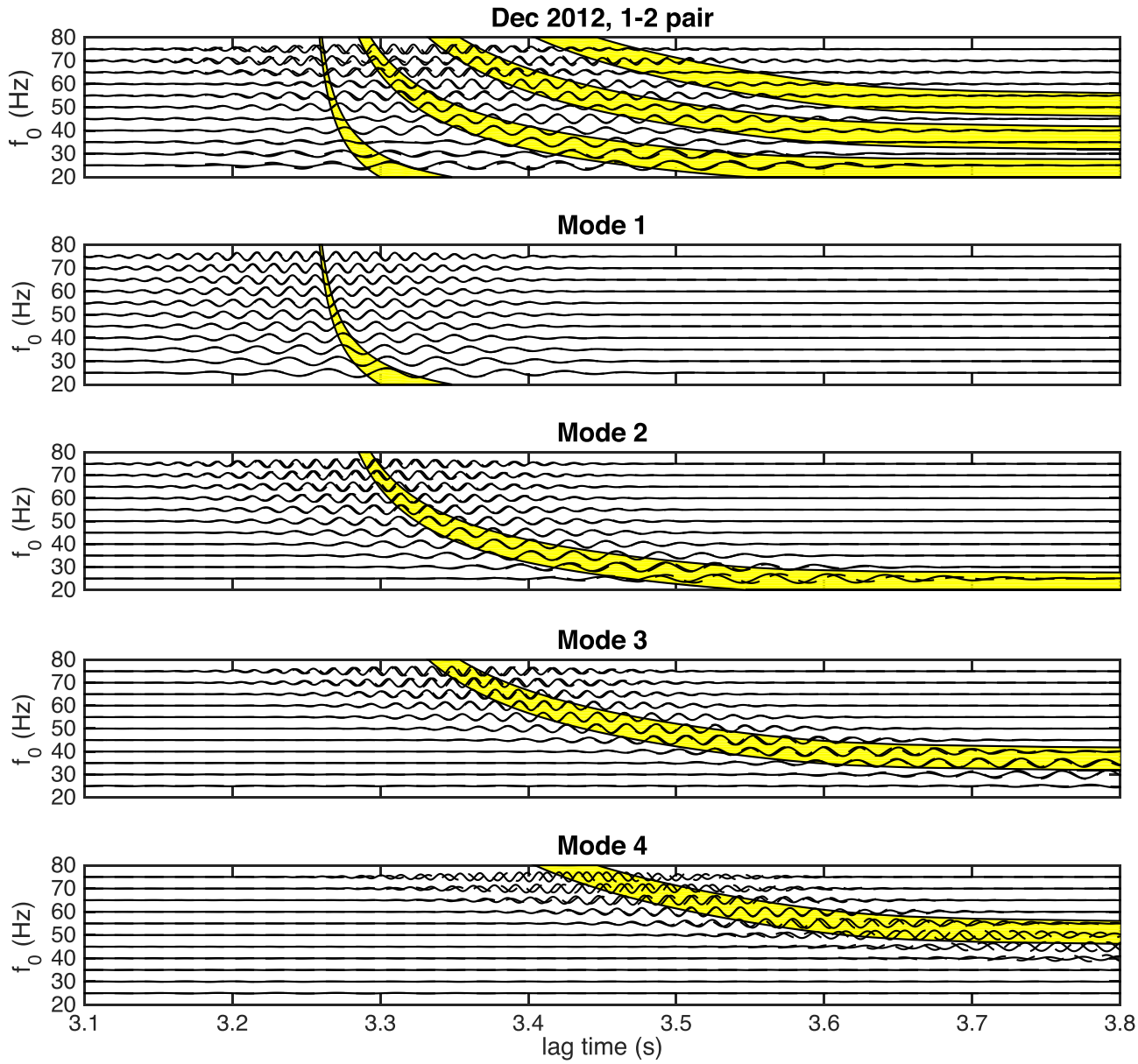

Figure 10. Solid and dashed lines are measured and simulated NCCFs, respectively, for the 1–2 instrument pair NCCF for the December 2012 experiment in overlapping 10 Hz frequency bands, 25 ± 5 Hz, 30 ± 5 Hz, . . . 75 ± 5 Hz. The shaded regions show the corresponding predicted bounds on dispersion curves, computed using the optimal eight-parameter model described in the text. In the upper panel all propagating modes that contribute to the wave field are included in the modal simulation. In the lower panels only modes with the identified mode number are included in the modal simulation. Individual data-based modal pulses were isolated using time-warping. Each narrowband NCCF, both data-based and simulated, is normalized to have the same maximum absolute amplitude.

conditions and environmental properties are advantageous for NI applications? Can inexpensive autonomous off-the-shelf instrumentation (clocks being the critical component) be used to perform ocean acoustic NI? The principal contribution of the work reported here is that partial answers to these questions are provided.

A simple conclusion to be drawn from the results presented in Sections 2 and 3 is that the feasibility of extracting estimates of weighted Green's functions using NI has been demonstrated in a coastal ocean environment with a depth of 100 m at ranges of 5 and 10 km, and that promising results have been presented in the same environment at 15 km range and in a 600 m deep coastal ocean environment at 5 km range. A more complete statement is much more nuanced, as described below. We emphasize that because coastal ocean propagation conditions are quite different than those in the deep ocean near the sound channel axis, the feasibility of NI at 10 km range in a coastal ocean environment should not be dismissed as uninteresting or insignificant in view of the recent demonstration (Woolfe *et al.* 2015; Woolfe & Sabra 2015) of NI at approximately 130 km range in the deep ocean.

Our reported success comes with several caveats. Before discussing the caveats, we mention the positive results that we have presented. The December 2012 NCCFs had relatively high SNR and were, to a good approximation, even functions of time (see also Mikesell *et al.* 2012; Colombi *et al.* 2014), apart from small current-induced timing shifts at both positive and negative lags. Given these desirable properties—which are consistent

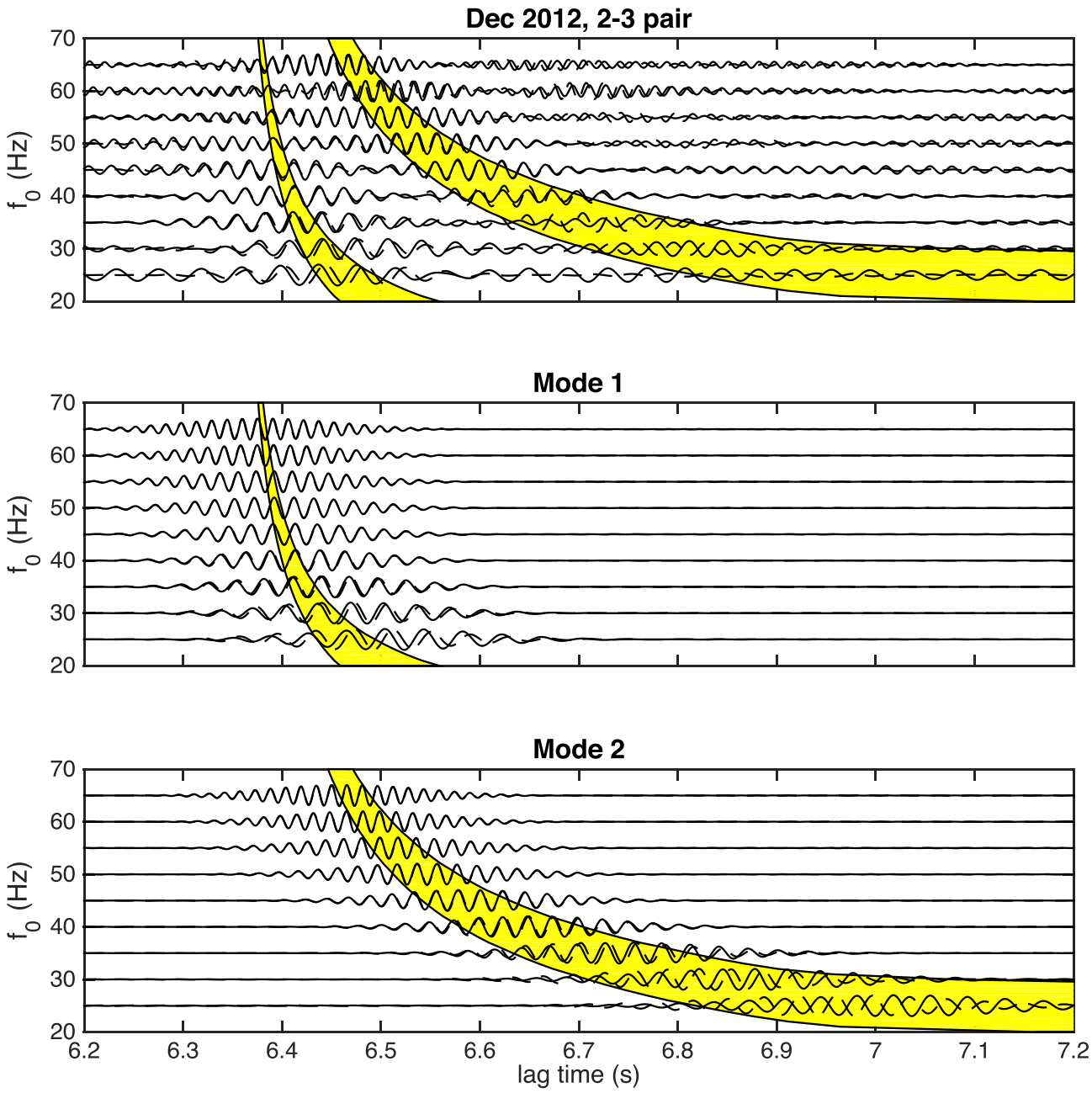

Figure 11. Same as Fig. 10, but for the 2–3 instrument pair in the frequency bands 25 ± 5 Hz, 30 ± 5 Hz, ... 65 ± 5 Hz.

with theoretical expectations—three types of phase-coherent processing were attempted and shown to be successful. Those three types of phase-coherent processing (waveform inversion, time-reversal/back-propagation, and time-warping) are well-established techniques to analyse high-quality data collected in active-source ocean acoustic experiments. Thus, our demonstration of the utility of those techniques serves to illustrate that NI-based estimates of NCCFs can be, from an information content perspective, as rich and useful as receptions in active-source experiments.

The NCCFs obtained in the September/October 2013 experiment were clearly inferior to those obtained in the December 2012 experiment. The September/October 2013 NCCFs computed using a sliding coherent integration time window were not stable over the entire duration of the experiment; as shown in Figs 5 and 6, coherent stacks over some time windows yielded one or two arrivals at the predicted travel time, but stacks over other time windows yielded no discernible ray arrivals. Furthermore, the de-phased NCCFs shown in Figs 5 and 6 reveal that for the 1–2 instrument pair negative lag structure (northward propagating energy) is much more energetic that positive lag structure (southward propagating energy), while for the 2–3 instrument pair, that is not true. There are two factors that probably contributed to the somewhat sporadic nature of the September/October 2013 NCCFs. First, owing to the very close proximity of that experiment to the core of the meandering Florida Current, the temporal variability of the environment during that experiment was probably much stronger than that during the December 2012 experiment. And second, owing to the closer proximity to the port of Miami during the September/October 2013 experiment, shipping noise during that experiment may have been much less laterally homogeneous and more sporadic than during the

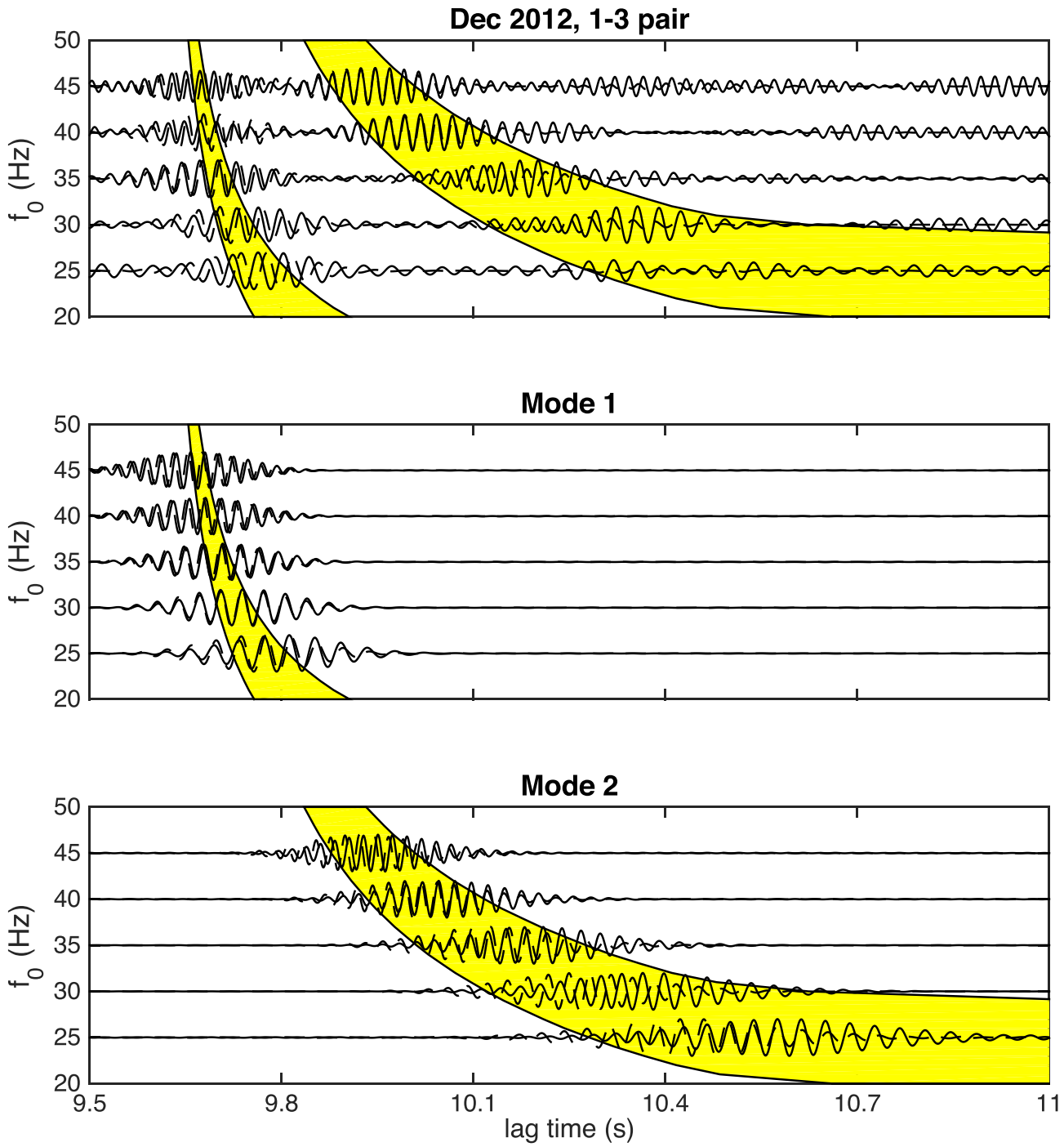

Figure 12. Same as Fig. 10, but for the 1–3 instrument pair in the frequency bands 25 ± 5 Hz, 30 ± 5 Hz, . . . 45 ± 5 Hz.

December 2012 experiment. As noted in Section 2, winds during the two experiments were not markedly different, leading us to expect that differences between the two experiments cannot be attributed to differences in wind conditions.

Another factor that may have contributed to the December 2012 NCCFs being of higher quality than the September/October 2013 NCCFs is the difference in the sound speed structure in the water column (recall Fig. 1). As we have discussed, the noise sources in our experiments were predominantly surface sources that excite steep angle energy at the surface much more strongly than flat angle energy. In both experiments, all paths connecting instrument pairs were bottom reflecting paths. Because the sediment sound speed exceeds the near-bottom water column sound speed, sound energy with small bottom grazing angles (less than the critical angle) experiences only very small loss on reflection, while steeper grazing angle energy is strongly attenuated on reflection. These comments lead to the expectation that the combination of large surface grazing angles and small bottom grazing angles, that is, an upward refracting sound speed profile, is desirable in ocean acoustic NI applications. In this regard, conditions in the successful December 2012 experiment were neutral, in the sense that the effectively constant water column sound speed was neither upward-refracting nor

downward-refracting. (Note, however, that all of the paths connecting receiver pairs in that experiment had bottom grazing angles smaller than the critical angle, consistent with our argument.) In contrast, in the largely disappointing September/October 2013 experiment ray paths were strongly downward refracting, leading to unfavourable NI conditions.

ACKNOWLEDGEMENTS

This work was supported by the US National Science Foundation, grants OCE1129860 and OCE1129524, and the US Office of Naval Research, grant N0001415122245.

REFERENCES

Bonnel, J. & Chapman, N.R., 2011. Geoacoustic inversion in a dispersive waveguide using warping operators, *J. acoust. Soc. Am.,* **130,** EL101–EL107.

Bonnel, J., Nicolas, B., Mars, J.I. & Walker, S.C., 2010. Estimation of modal group velocities with a single receiver for geoacoustic inversion in shallow water, *J. acoust. Soc. Am.* **128,** 719–727.

Bonnel, J., Dosso, S.E. & Chapman, N.R., 2013. Bayesian geoacoustic inversion of single hydrophone light bulb data using warping dispersion analysis, *J. acoust. Soc. Am.,* **134,** 120–130.

Boschi, L. & Weemstra, C., 2015. Stationary-phase integrals in the cross-correlation of ambient noise, *Rev. Geophys.,* **53,** 411–451.

Brooks, L.A. & Gerstoft, P., 2009. Green's function approximation from cross-correlations of 20–100 Hz noise during a tropical storm, *J. acoust. Soc. Am.,* **125,** 723–734.

Brown, M.G. & Lu, C., 2016, Green's function retrieval in a field of random water waves, *Wave Motion,* **60,** 8–19.

Brown, M.G., Viechnicki, J. & Tappert, F.D., 1996. On the measurement of modal group time delays in the deep ocean, *J. acoust. Soc. Am.,* **100,** 2093–2102.

Brown, M.G., Godin, O.A., Williams, N.J., Zabotin, N.A., Zabotina, L. & Banker, G.J., 2014. Acoustic Green's function extraction from ambient noise in a coastal ocean environment, *Geophys. Res. Lett.,* **41,** 5555–5562.

Burov, V.A., Grinyuk, A.V., Kravchenko, V.N., Mukhanov, P.Yu., Sergeev, S.N. & Shurup, A.S., 2014. Selection of modes from a shallow-water noise field by single bottom hydrophones for passive tomography purposes, *Acoust. Phys.,* **60,** 647–656.

Campillo, M. & Paul, A., 2003. Long-range correlations in the diffuse seismic coda, *Science,* **299,** 547–549.

Campillo, M. & Roux, P., 2014. Seismic imaging and monitoring with ambient noise correlations, in *Treatise of Geophysics,* vol. 1, pp. 256–271, eds Romanowicz, B. & Dziewonski, A., Elsevier.

Colombi, A., Boschi, L., Roux, P. & Campillo, M., 2014. Green's function retrieval through cross-correlations in a two-dimensional complex reverberating medium, *J. acoust. Soc. Am,* **135,** 1034–1043.

Duvall, T.L., Jr, Jeffferies, S.M., Harvey, J.W. & Pomerantz, M.A., 1993. Time-distance helioseismology, *Nature,* **362,** 430–432.

Edelman, G.F., Akal, T., Hodgkiss, W.S., Kim, S., Kuperman, W.A. & Song, H.C., 2002. An initial demonstration of underwater communication using time-reversal, *IEEE J. Ocean. Eng.,* **27,** 602–609.

Fink, M., Cassereau, D., Derode, A., Prada, C., Roux, P., Tanter, M., Thomas, J.-L. & Wu, F., 2000. Time-reversed acoustics, *Rep. Prog. Phys.,* **63,** 1933–1995.

Fricke, J.T., Evers, L.G., Smets, P.S.M., Wapenaar, K. & Simons, D.G., 2014. Infrasonic interferometry applied to microbaroms observed at the Large Aperture Infrasound Array in the Netherlands, *J. geophys. Res.,* **119,** 9654–9665.

Fried, S.E., Kuperman, W.A., Sabra, K.G. & Roux, P., 2008. Extracting the local Green's function on a horizontal array from ambient ocean noise, *J. acoust. Soc. Am.,* **124,** EL183–EL188.

Garnier, J. & Papanicolaou, J., 2009. Passive sensor imaging using cross correlations of noisy signals in a scattering medium, *SIAM J. Imaging Sci.,* **2,** 396–437.

Gerstoft, P., Hodgkiss, W.S., Siderius, M. & Harrison, C.H., 2008. Passive fathometer processing, *J. acoust. Soc. Am.,* **123,** 1297–1305.

Godin, O.A., 2006. Recovering the acoustic Green's function from ambient noise cross-correlation in an inhomogeneous moving medium, *Phys. Rev. Lett.,* **97,** 054301, doi:10.1103/PhysRevLett.97.054301.

Godin, O.A., 2009. Retrieval of Green's functions of elastic waves from thermal fluctuations of fluid-solid systems, *J. acoust. Soc. Am.,* **125,** 1960–1970.

Godin, O.A., Zabotin, N.A. & Goncharov, V.V., 2010. Ocean tomography with acoustic daylight, *Geophys. Res. Lett.,* **37,** L13605, doi:10.1029/2010GL043623.

Godin, O.A., Irisov, V.G. & Charnotskii, M.I., 2014a. Passive acoustic measurements of wind velocity and sound speed in air, *J. acoust. Soc. Am.,* **135**(2), EL68–EL74.

Godin, O.A., Zabotin, N.A., Sheehan, A.F. & Collins, J.A., 2014b. Interferometry of infragravity waves off New Zealand, *J. geophys. Res.,* **118**(2), 1103–1122.

Godin, O.A., Brown, M.G., Zabotin, N.A., Zabotina, L. & Williams, N.J., 2014c. Passive acoustic measurement of flow velocity in the Straits of Florida, *Geosci. Lett.,* **1,** doi:10.1186/s40562-014-0016-6.

Godin, O.A., Katsnelson, B.G., Qin, J., Brown, M.G., Zabotin, N.A. & Zang, X., 2016. Application of time reversal to passive acoustic remote sensing of the ocean, *Acoust. Phys.,* submitted.

Gorbatov, A., Saygin, E. & Kennett, B.L.N., 2013. Crustal properties from seismic station autocorrelograms. *Geophys. J. Int.,* **192,** 861–870.

Haney, M.M., 2009. Infrasonic ambient noise interferometry from correlations of microbaroms, *Geophys. Res. Lett.,* **36,** L19808, doi:10.1029/2009GL040179.

Jackson, D.R. & Dowling, D.R., 1991. Phase-conjugation in underwater acoustics, *J. acoust. Soc. Am.,* **89,** 171–181.

Kim, J. & Choi, J.W., 2014. Adaptive passive fathometer processing of surface-generated noise received by Nested array, *J. acoust. Soc. Am.,* **136,** 2149–2149.

Kuperman, W.A., Hodgkiss, W.S., Song, H.C., Akal, T., Ferla, C. & Jackson, D.R., 1998. Phase conjugation in the ocean: experimental demonstration of an acoustic time-reversal mirror, *J. acoust. Soc. Am.,* **103,** 25–40.

Lani, S.W., Sabra, K.G., Hodgkiss, W.S., Kuperman, W.A. & Roux, P., 2013. Coherent processing of shipping noise for ocean monitoring, *J. acoust. Soc. Am.,* **133,** EL108–EL113.

Lobkis, O.I. & Weaver, R.L., 2001. On the emergence of the Green's function in the correlations of a diffuse field, *J. acoust. Soc. Am.,* **110,** 3011–3017.

Mikesell, T.D., van Wijk, K., Blum, T.E., Snieder, R. & Sato, H., 2012. Analyzing the coda from correlating scattered surface waves, *J. acoust. Soc. Am,* **131,** EL275–EL281.

Munk, W., Worcester, P. & Wunsch, C., 1995. *Ocean Acoustic Tomography,* Cambridge Univ. Press.

Porter, M.B., 1997. The KRAKEN normal mode program, http://oalib/hlsresearch.com/Modes/kraken.pdf

Rickett, J.E. & Claerbout, J.F., 2000. Calculation of the Sun's impulse response by multi-dimensional spectral factorization, *Sol. Phys.,* **192,** 203–210.

Roux, P. & Kuperman, W.A., 2005. Time reversal of ocean noise, *J. acoust. Soc. Am.,* **117,** 131–136.

Roux, P., Kuperman, W.A. & the NPAL Group, 2004. Extracting coherent wave fronts from acoustic ambient noise in the ocean, *J. acoust. Soc. Am.,* **116,** 1995–2003.

Rytov, S.M., Kravtsov, Yu.A. & Tatarskii, V.I., 1989. *Principles of Statistical Radiophysics. 3: Elements of Random Fields,* Springer.

Sabra, K.G., Roux, P. & Kuperman, W.A., 2005. Emergence rate of the time-domain Green's function from the ambient noise cross-correlation function, *J. acoust. Soc. Am.,* **118,** 3524–3531.

Sabra, K.G., Winkel, E.S., Bourgoyne, D.A., Elbing, B.R., Ceccio, S.L., Perlin, M. & Dowling, D.R., 2007a. On using cross-correlation of turbulent flow-induced ambient vibrations to estimate the structural impulse

response. Application to structural health monitoring, *J. acoust. Soc. Am.,* **121,** 1987–2005.

Sabra, K.G., Conti, S., Roux, P. & Kuperman, W.A., 2007b. Passive in vivo elastography from skeletal muscle noise, *Appl. Phys. Lett.,* **90,** 194101, doi:10.1063/1.2737358.

Sabra, K.G., Fried, S., Kuperman, W.A. & Prior, M., 2013. On the coherent components of low-frequency ambient noise in the Indian Ocean, *J. acoust. Soc. Am.,* **133,** EL20–EL25.

Shapiro, N.M., Campillo, M., Stehly, L. & Ritzwoller, M., 2005. High resolution surface wave tomography from ambient seismic noise, *Science,* **307,** 1615–1618.

Siderius, M., Harrison, C.H. & Porter, M.B., 2006. A passive fathometer technique for imaging seabed layering using ambient noise, *J. acoust. Soc. Am.,* **120,** 1315–1323.

Siderius, M., Song, H., Gerstoft, P., Hodgkiss, W.S., Hursky, P. & Harrison, C., 2010. Adaptive passive fathometer processing, *J. acoust. Soc. Am.,* **127,** 2193–2200.

Snieder, R., 2004. Extracting the Green's function from the correlation of coda waves: a derivation based on stationary phase, *Phys. Rev. E,* **69,** 046610, doi:10.1103/PhysRevE.69.046610.

Snieder, R. & Larose, E., 2013. Extracting Earth's elastic wave response from noise measurements. *Ann. Rev. Earth Planet. Sci.,* **41,** 183–206.

Udovydchenkov, I.A. & Brown, M.G., 2008. Modal group time spreads in weakly range-dependent deep ocean environments, *J. acoust. Soc. Am.,* **123,** 41–50.

Wapenaar, K., 2004. Retrieving the elastodynamic Green's function of an arbitrary inhomogeneous medium by cross correlation, *Phys. Rev. Lett.,* **93,** 254301, doi:10.1103/PhysRevLett.93.254301.

Weaver, R.L. & Lobkis, O.I., 2005. Fluctuations in diffuse field-field correlations and the emergence of the Green's function in open systems, *J. acoust. Soc. Am.,* **117,** 3432–3439.

Woolfe, K.G. & Sabra, K.G., 2015. Variability of the coherent arrivals extracted from low-frequency deep-ocean ambient noise correlations, *J. acoust. Soc. Am.,* **138,** 521–532.

Woolfe, K.F., Lani, S. & Sabra K.G. & Kuperman, W.A., 2015. Monitoring deep-ocean temperatures using acoustic ambient noise, *Geophys. Res. Lett.,* **42,** 2878–2884.

Yang, Y., Ritzwoller, M.H., Levshin, A.L. & Shapiro, N.M., 2007. Ambient noise Rayleigh wave tomography across Europe, *Geophys. J. Int.,* **168,** 259–274.

Yardim, C., Gerstoft, P., Hodgkiss, W.S. & Traer, J., 2014. Compressive geoacoustic inversion using ambient noise, *J. acoust. Soc. Am.,* **135,** 1245–1255.

Zabotin, N.A. & Godin, O.A., 2011. Emergence of acoustic Green's functions from time averages of ambient noise, *Acta Acust. United Acust.,* **97,** 44–53.

Zang, X., Brown, M.G. & Godin, O.A., 2015. Waveform modeling and inversion of ambient noise cross-correlation functions in a coastal ocean environment, *J. acoust. Soc. Am.,* **138,** 1325–1333.